

# Topology optimization of stiff structures under self-weight for given volume using a smooth Heaviside function

P. Kumar<sup>1</sup>

*Department of Mechanical Engineering, Indian Institute of Science, Bengaluru 560012, Karnataka, India*

---

**Abstract:** This paper presents a density-based topology optimization approach to design structures under self-weight load. Such loads change their magnitude and/or location as the topology optimization advances and pose several unique challenges, e.g., non-monotonous behavior of compliance objective, parasitic effects of the low-stiffness elements and unconstrained nature of the problems. The modified SIMP material interpolation in conjunction with the three-field density representation technique (original, filtered and projected design fields) is employed to achieve optimized solutions close to 0-1. Thus, parasitic effects of low-stiffness elements are circumvented. The mass density of each element is interpolated via a smooth Heaviside function yielding continuous transition between solid and void states of elements. This helps formulate a constraint on the maximum magnitude of the self-weight for the given volume in a such a manner that which implicitly imposes a lower bound on the permitted volume. The propose approach maintains the constrained nature of the optimization problem. Load sensitivities are evaluated using the adjoint-variable method. Compliance of the domain is minimized to achieve the optimized designs using the Method of Moving Asymptotes. Efficacy and robustness of the presented approach is demonstrated by designing various 2D and 3D structures involving self-weight.

**Keywords:** Topology optimization; Self-weight; Design-dependent loads; Heaviside projection function; Compliance minimization

---

## 1 Introduction

Topology optimization (TO) is gaining popularity day-by-day as a design tool to find the optimized material distributions for a wide range of problems including single- and/or multi-physics concepts (Sigmund and Maute, 2013). Such problems that involve self-weight, a design-dependent force (Kumar et al., 2020), can provide various distinctive challenges, e.g., (1) non-monotonous characteristics of the compliance objective with respect to the design variables, (2) tendency to lose constrained nature of the compliance optimization problem with a given resource constraint and (3) the parasitic effects of low-stiffness elements (Bruyneel and Duysinx, 2005), which are also noted in maximization of eigenvalues using TO when the Solid Isotropic Material with Penalization (SIMP) formulation is employed (Pedersen, 2000). Civil engineering structures typically encounter self-weight and thus, their performance can be directly associated with the location of optimized material distribution (Bruyneel and Duysinx, 2005). In addition, consideration of the self-weight can become essential for large-scale structures. Herein, the motif is to present a density-based TO approach covering all the above mentioned challenges to

---

<sup>1</sup>prabhatk@iisc.ac.in; prabhatkumar.rns@gmail.com

optimize structures subject to self-weight. In a typical density-based TO approach, each finite element (FE) is assigned a design variable (material density)  $x \in [0, 1]$  that is assumed to be constant within the element.  $x = 1$  and  $x = 0$  indicate the solid and void phases of the element, respectively.

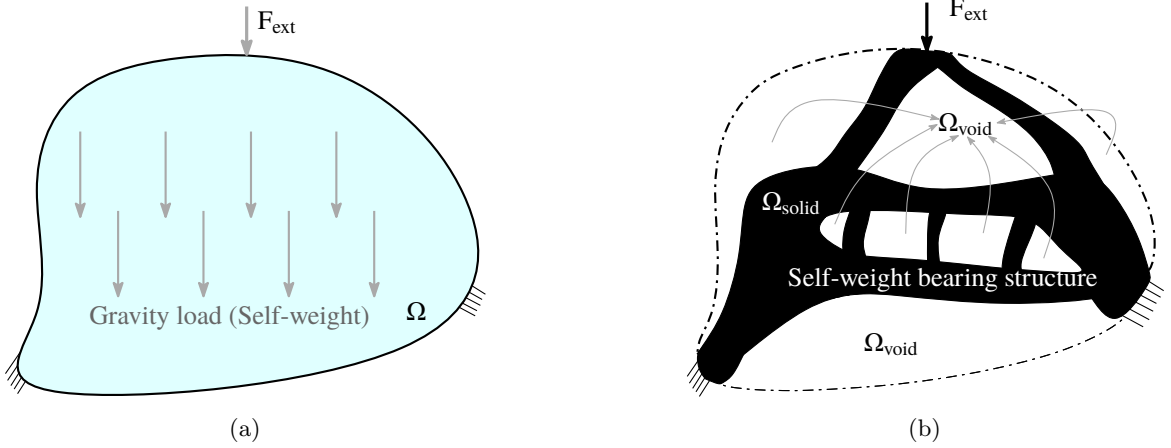


Figure 1: (a) Schematic diagram of a 2D design optimization problem with self-weight and external load  $F_{\text{ext}}$ . Presence of external load may not always be necessary. (b) A representative solution to the design problem shown in (a).  $\Omega$ ,  $\Omega_{\text{solid}}(\bar{x} = 1)$  and  $\Omega_{\text{void}}(\bar{x} = 0)$  represent the actual design domain, the optimized material layout design (self-weight bearing structure) and void domain, respectively.  $\bar{x}_e$  indicates the physical material density of element  $e$  in the parameterized setting.

Design-dependent loads typically alter their location, magnitude and/or direction as TO progresses and therefore, their sensitivities with respect to the design variables need to be accounted in the TO formulation (Kumar and Langelaar, 2021; Kumar et al., 2020). In such loading scenarios, the overall sensitivities of the compliance objective with respect to the design variables no more remain always negative (see Sec. 3.2) and hence, compliance loses its most cherished monotonic characteristics (Bruyneel and Duysinx, 2005). A numerical solution to a purely self-weight-loaded design for compliance minimization can be feasible even when  $\bar{x}_e \rightarrow 0 \forall e|_{e=1,2,3,\dots,\text{Nel}}$ , i.e., compliance becomes approximately equal to zero as it is being minimized. However, such a solution is nonsensical as per mechanical viewpoint and also, makes problem unconstrained (Bruyneel and Duysinx, 2005). Note, Nel is the total FEs employed to parameterize the design domain  $\Omega$  (Fig. 1a). The parasitic effects are due to low-stiffness elements wherein ratio between– gravity force to design variables and stiffness to design variables tend to become unbounded (Bruyneel and Duysinx, 2005). The proposed approach systematically offers a solution to the above mentioned anomalies and provides the optimized solutions close to 0-1. A schematic diagram for a 2D structure<sup>2</sup> experiencing self-weight (gravity load) and external constant load  $F_{\text{ext}}$  is depicted in Fig. 1a. A possible solution to the problem (Fig. 1a) is displayed in Fig. 1b. It can be noted that location and magnitude of the gravity load change, which pose challenges in a TO formulation. Next, we review the TO approaches presented for structures subject to self-weight.

In a structural optimization framework self-weight was accounted first by Rozvany (1977). Subsequently, several researchers have presented their TO approaches including self-weight. Bruyneel and Duysinx (2005) identified challenges in a continuum-based TO framework with self-weight. They found that when the design variables attain their lower bounds then the ratio between the mass density (gravity load or self-weight) and the material stiffness obtained via the SIMP formulation tends to infinity. Consequently, displacements become unbounded and that

<sup>2</sup>2D structure diagram is taken for the simplicity.

in-turn makes compliance unbounded. As a result, the optimized designs contain many gray elements ( $0 < \bar{x} < 1$ ). To subdue such unrealistic gray material that causes parasitic effects, they altered the SIMP formulation using a threshold density value  $\bar{x}_{th}$  wherein the material stiffness is regarded linear below  $\bar{x}_{th}$ , which introduces non-differentiability in the material model. This paper however shows that with the modified SIMP material model (Sigmund, 2007), a smooth interpolation scheme, in conjunction with the three-field density technique (Lazarov et al., 2016), parasitic effects can be circumvented. Lee et al. (2012) employed the approach presented by Bruyneel and Duysinx (2005) in their stress-constrained-based TO method for design-dependent loads. Huang and Xie (2011) used the bi-directional evolutionary structural optimization approach with the RAMP material model (Stolpe and Svanberg, 2001) for designing structures subject to self-weight. Xu et al. (2013) proposed the guide-weight approach using the optimality criteria method. They employed the SIMP and the RAMP material models to demonstrate their approach. Chang and Chen (2014) presented a modified gradient projection method to solve problems involving density-dependent forces. Holmberg et al. (2015) employed the non-linear semi-definite programming for the worst-case TO with self-weight. A closed B-splines-based approach was proposed by Zhang et al. (2017) to avoid parasitic effects of low-density regions for design-dependent loads. Félix et al. (2020) employed a power-law function for the material density interpolation to reduce the parasitic effects. Zhang et al. (2021) modified the SIMP model and used a sequence of penalty factor in their approach. They proposed a multi-objective TO approach wherein the objective is the weighted sum of the strain energy and displacements of the structures. Novotny et al. (2021) proposed a topological derivative-based TO approach using a regularized formulation for imposing feasible volume constraints for structures under self-weight.

This paper presents an approach using the standard density-based TO with the modified SIMP scheme in conjunction with the three-field density representation technique (original, filtered and projected design fields, cf. Lazarov et al. (2016)) for the design problems involving self-weight. The parameter  $\beta$  associated with the three-field technique is updated using a continuation scheme to achieve the optimized designs close to 0-1 and thereby, parasitic effects arising due to the low-stiffness regions are circumvented. A smooth Heaviside function is employed to interpolate the mass density of each element, which provides a continuous transition between the void and solid states of the element. In addition, it helps formulate a constraint on the maximum magnitude of the self-weight using the given volume fraction of the domain in such a manner that a lower bound on the resource constraint is imposed implicitly. Consequently, the tendency to lose constrained nature of problem is subdued. Load sensitivities are evaluated using the computationally cheap adjoint-variable method. Compliance is minimized to obtain the optimized material layouts of various structures subject to self-weight with different boundary specifications using the Method of Moving Asymptotes (Svanberg, 1987). The approach is readily extended for three-dimensional problems, which is demonstrated by solving two 3D numerical examples.

The layout of this paper is organized as follows. Section 2 describes the modeling of self-weight using a smooth Heaviside function. Problem description including the topology optimization formulation and sensitivity analysis is presented in Section 3. Next, numerical examples for various 2D and 3D design problems involving self-weight are presented in Section 4. Pertinent discussions are presented, and a study for different parameters are presented. Section 4.3 presents three-dimensional results. Lastly, conclusions are drawn in Section 5.

## 2 Self-weight modeling

Self-weight  $\mathbf{f}_g$  arises due to the gravitational acceleration  $\mathbf{g}$ , which acts vertically downward. In a continuum setting,  $\mathbf{f}_g$  can be determined as

$$\mathbf{f}_g = \gamma V \mathbf{g} = \gamma V g \mathbf{e}, \quad (1)$$

where  $\gamma$  ( $\text{kg m}^{-3}$ ) is mass density of the material used,  $V$  ( $\text{m}^3$ ) represents volume of the domain, and  $\mathbf{g} = g \mathbf{e} = -9.81 \text{ m s}^{-2} \mathbf{e}$ , where  $g = -9.81 \text{ m s}^{-2}$  and  $\mathbf{e}$ , a unit vector, directs in positive  $y$ - and  $z$ -directions for 2D and 3D settings respectively.

In a discrete setting, the elemental self-weight  $\mathbf{f}_g^e$  is evaluated as (Cook et al., 2007)

$$\mathbf{f}_g^e = \begin{cases} \int_{\Omega_e} \gamma_e \mathbf{N}^\top \begin{Bmatrix} 0 \\ g \end{Bmatrix} dV = \gamma_e \int_{\Omega_e} \mathbf{N}^\top \begin{Bmatrix} 0 \\ g \end{Bmatrix} dV, & (\text{For 2D}) \\ \int_{\Omega_e} \gamma_e \mathbf{N}^\top \begin{Bmatrix} 0 \\ 0 \\ g \end{Bmatrix} dV = \gamma_e \int_{\Omega_e} \mathbf{N}^\top \begin{Bmatrix} 0 \\ 0 \\ g \end{Bmatrix} dV, & (\text{For 3D}) \end{cases} \quad (2)$$

where  $\mathbf{N} = [N_1 \mathbf{I}, \dots, N_{N_{\text{no}}} \mathbf{I}]$ .  $\mathbf{I}$  is the identity matrix in  $\mathcal{R}^n$ ,  $n$  indicates dimension of the domain wherein  $n = 2$  and  $n = 3$  for 2D and 3D cases respectively. Nno is the total number of nodes per element employed to discretize the design domain. We use four-noded quadrilateral and eight-noded hexahedral finite elements (FEs)  $\Omega_e$  to describe the two- and three-dimensional design domains respectively, i.e,  $N_{\text{no}} = 4$  (2D) and  $N_{\text{no}} = 8$  (3D).

In a typical TO framework, each finite element displays solid ( $\bar{x}_e = 1$ ) and void ( $\bar{x}_e = 0$ ) material phases;  $\bar{x}_e$  denotes the physical material variable of element  $e$  (see Sec. 3). Herein, the material density  $\gamma_e$  of each FE is related to  $\bar{x}_e$  wherein elements with  $\bar{x}_e = 0$  and  $\bar{x}_e = 1$  have  $\gamma_e = \gamma_e^v$  (mass density of void FE) and  $\gamma_e = \gamma_e^s$  (mass density of solid FE) material density respectively. A smooth Heaviside function is employed to evaluate the material density of each FE using its both states that offers continuous transition between the phases of the element as TO progresses. In addition, it helps (i) evaluate the load sensitivities (see Sec.3.2) readily using the adjoint-variable method and (ii) formulate a constraint using the maximum amount of self-weight permitted that implicitly provides a lower bound on the resource volume and at the end of the TO iteration the volume constraint is noted active (see Sec. 4.1.1). Mathematically, the mass density interpolation is written as

$$\gamma_e = \gamma_e^v + (\gamma_e^s - \gamma_e^v) H(\bar{x}_e, \eta_\gamma, \beta_\gamma), \quad (3)$$

where  $\chi = \frac{\gamma_e^v}{\gamma_e^s} = 1e^{-9}$  is used;  $\chi$  is termed the mass density contrast. The smooth Heaviside projection function  $H(\bar{x}_e, \eta_\gamma, \beta_\gamma)$  is defined using the physical design variables as (Wang et al., 2011)

$$H(\bar{x}_e, \eta_\gamma, \beta_\gamma) = \frac{\tanh(\beta_\gamma \eta_\gamma) + \tanh(\beta_\gamma (\bar{x}_e - \eta_\gamma))}{\tanh(\beta_\gamma \eta_\gamma) + \tanh(\beta_\gamma (1 - \eta_\gamma))}, \quad (4)$$

where both  $\eta_\gamma$  and  $\beta_\gamma$  are adjustable parameters that provide the position of step and the slope.  $\eta_\gamma$  and  $\beta_\gamma$  are called the mass density parameters. Fig. 2 depicts mass density interpolation function for different  $\eta_\gamma$  and  $\beta_\gamma$ . For higher  $\beta_\gamma$  more sharpness can be noted (Fig. 2).

In view of shape functions of quadrilateral (2D) and hexahedral (3D) elements in association with the Gauss-quadrature points, (2) gives (Cook et al., 2007)

$$\mathbf{f}_g^e = \gamma_e^s (\chi + (1 - \chi) H(\bar{x}_e, \eta_\gamma, \beta_\gamma)) L_g V_e, \quad (5)$$

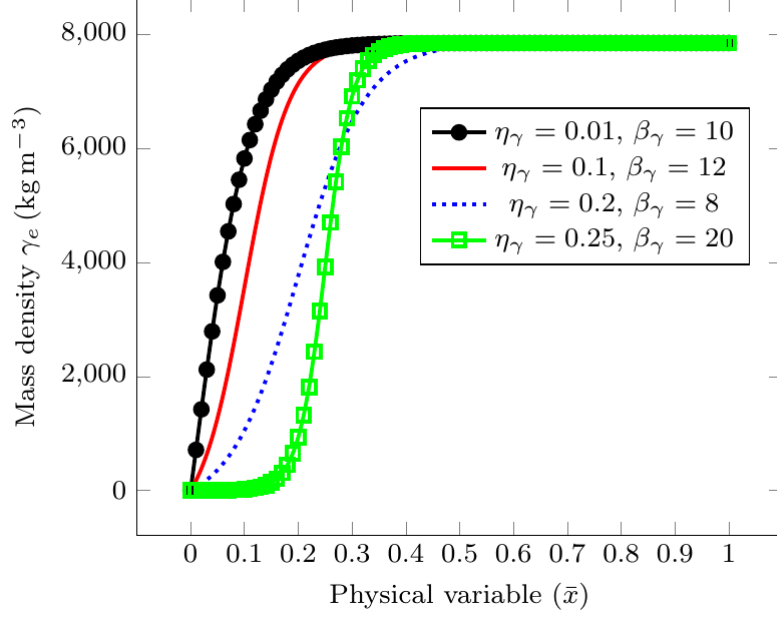


Figure 2: Mass density interpolation plot

where  $L_g = [0, \frac{g}{4}, 0, \frac{g}{4}, 0, \frac{g}{4}, 0, \frac{g}{4}]^\top$  and

$$L_g = \left[ 0, 0, \frac{g}{8}, 0, 0, \frac{g}{8}, 0, 0, \frac{g}{8}, 0, 0, \frac{g}{8}, 0, 0, \frac{g}{8}, 0, 0, \frac{g}{8}, 0, 0, \frac{g}{8} \right]^\top$$

for 2D and 3D settings respectively, and  $V_e = \frac{V}{Nel} = \frac{L_x L_y t}{Nel}$  (2D),  $V_e = \frac{V}{Nel} = \frac{L_x L_y L_z}{Nel}$  (3D).  $L_x, L_y, L_z$  and  $t$  represent the length, width, height and thickness of the design domain. The derivatives of gravity force  $\mathbf{f}_g^e$  with respect to  $\bar{x}_e$  can be readily evaluated as

$$\frac{\partial \mathbf{f}_g^e}{\partial \bar{x}_e} = \gamma_e^s \left( \chi + (1 - \chi) \frac{\partial H(\bar{x}_e, \eta_\gamma, \beta_\gamma)}{\partial \bar{x}_e} \right) L_g V_e, \quad (6)$$

where

$$\frac{\partial H(\bar{x}_e, \eta_\gamma, \beta_\gamma)}{\partial \bar{x}_e} = \beta_\gamma \frac{1 - \tanh(\beta_\gamma(\bar{x}_e - \eta_\gamma))^2}{\tanh(\beta_\gamma \eta_\gamma) + \tanh(\beta_\gamma(1 - \eta_\gamma))}.$$

Finally, the elemental forces are assembled to determine the total (global) gravity load  $\mathbf{F}_g$  experienced by the design in a discrete setting and thus, compliance of the domain and  $\frac{\partial \mathbf{F}_g}{\partial \bar{\mathbf{x}}}$  are evaluated. Next, the problem formulation is presented.

### 3 Problem formulation

The density-based topology optimization in conjunction with the three-field density formulation (Lazarov et al., 2016) is used in the presented approach. For the material interpolation, the modified SIMP formulation (Sigmund, 2007) is employed that relates modulus of elasticity  $E_e$  of element  $e$  to its physical design variable  $\bar{x}_e$  using the power law as

$$E_e(\bar{x}_e) = E_e^v + (E_e^s - E_e^v) (\bar{x})^p, \quad (7)$$

where  $E_e^v$  and  $E_e^s$  are the Young's moduli of the void and the solid phases of element  $e$ , respectively. The material contrast, i.e.  $\frac{E_e^v}{E_e^s} = 1 \times 10^{-6}$  is set and  $p$ , the SIMP penalty parameter, is set to 3 that guides TO convergence towards '0-1' designs.

In the three-field  $(\mathbf{x}, \tilde{\mathbf{x}}, \bar{\mathbf{x}})$  density representation technique (Lazarov et al., 2016),  $\mathbf{x}$ ,  $\tilde{\mathbf{x}}$  and  $\bar{\mathbf{x}}$  denote vectors containing the original design variables  $x_e$ , filtered design variables  $\tilde{x}_e$  and physical design variables  $\bar{x}_e$  respectively. The chain of transformation between these variables can be denoted via  $x_e \rightarrow \tilde{x}_e \rightarrow \bar{x}_e$  (Lazarov et al., 2016).

The filtered variables  $\tilde{x}_e$ , determined using a mesh-independent density filtering scheme (Bruns and Tortorelli, 2001), is given as

$$\tilde{x}_e = \frac{\sum_{i=1}^{nne} v_i x_i w(\mathbf{x}_i)}{\sum_{i=1}^{nne} v_i w(\mathbf{x}_i)}, \quad (8)$$

where  $nne$  indicates the total number of neighboring elements of element  $e$ ,  $v_i$  is the volume of the element  $i$ .  $w(\mathbf{x}_i)$ , the weight function, is determined using the Euclidean distance between the centroids  $\mathbf{x}_e$  and  $\mathbf{x}_i$  of elements  $e$  and  $i$  as

$$w(\mathbf{x}_i) = \max \left( 0, 1 - \frac{\|\mathbf{x}_e - \mathbf{x}_i\|}{r_{\text{fill}}} \right), \quad (9)$$

where  $r_{\text{fill}}$  is the employed filter radius. The derivatives of  $\tilde{x}_e$  with respect to  $x_i$  is calculated as

$$\frac{\partial \tilde{x}_e}{\partial x_i} = \frac{v_i w(\mathbf{x}_i)}{\sum_{j=1}^{nne} v_j w(\mathbf{x}_j)}. \quad (10)$$

The physical design variable  $\bar{x}_e$ , determined using corresponding filtered variable  $\tilde{x}_e$  and a smooth Heaviside function which is analogous to (4), is given as

$$\bar{x}_e = H(\tilde{x}_e, \beta, \eta)|_{\eta=0.5} = \frac{\tanh(\frac{\beta}{2}) + \tanh(\beta(\tilde{x}_e - \frac{1}{2}))}{2 \tanh(\frac{\beta}{2})} \quad (11)$$

where  $\beta \in [1, \infty)$  controls the sharpness of the Heaviside function  $H(\tilde{x}_e, \beta, \eta)$ . Typically  $\beta$  is increased in a continuation fashion from its initial value  $\beta_i = 1$  to maximum value  $\beta_{\text{max}}$  to achieve the solution close to 0-1 (Wang et al., 2011). In turn, parasitic effects of the low-density element can be suppressed. Herein,  $\beta_{\text{max}} = 256$  is set, and is doubled after every 25 optimization iterations. With  $\eta = 0$  and  $\eta = 1$ , one achieves the minimum length scale on the void and solid phase respectively (Trillet et al., 2021; Wang et al., 2011), and also, attains the Heaviside approximation given by Guest et al. (2004) and Sigmund (2007) respectively. One determines the derivative of  $\bar{x}_e$  with respect to  $\tilde{x}_e$  as

$$\frac{\partial \bar{x}_e}{\partial \tilde{x}_e} = \beta \frac{1 - \tanh(\beta(\tilde{x}_e - \frac{1}{2}))^2}{2 \tanh(\frac{\beta}{2})}. \quad (12)$$

Using the chain rule, the derivative of a function  $f$  with respect to the actual design variable can be determined in view of (10) and (12) as

$$\frac{\partial f}{\partial x_i} = \sum_{e=1}^{nne} \frac{\partial f}{\partial \bar{x}_e} \frac{\partial \bar{x}_e}{\partial \tilde{x}_e} \frac{\partial \tilde{x}_e}{\partial x_i}, \quad (13)$$

wherein  $\frac{\partial f}{\partial \bar{x}_e}$  can be determined for the given objective function (see Sec. 3.2).

### 3.1 Topology optimization formulation

The compliance (strain energy) of the structures subject to self-weight and/or external constant load is minimized to obtain the optimized topologies. The optimization problem is formulated as

$$\left. \begin{aligned} \min_{\bar{\mathbf{x}}(\mathbf{x})} \quad & f_0 = 2SE = (\mathbf{F}_g(\bar{\mathbf{x}}) + \kappa \mathbf{F}_{\text{ext}})^\top \mathbf{u}(\bar{\mathbf{x}}) \\ \text{Subject to:} \quad & \\ \boldsymbol{\lambda} : \quad & \mathbf{K}(\bar{\mathbf{x}}) \mathbf{u}(\bar{\mathbf{x}}) = \mathbf{F}_g(\bar{\mathbf{x}}) + \kappa \mathbf{F}_{\text{ext}} \\ \Lambda_1 : \quad & g_1 \equiv V(\bar{\mathbf{x}}) \leq V^* \\ \Lambda_2 : \quad & g_2 \equiv F_g^{\max} \leq \sum_{e=1}^{\text{Nel}} F_g^e \\ & \mathbf{0} \leq \bar{\mathbf{x}} \leq \mathbf{1} \\ \text{Data:} \quad & V^*, \mathbf{F}_{\text{ext}}, \gamma_s, g, L_x, L_y, L_z, t, E_e^s, \kappa \end{aligned} \right\}, \quad (14)$$

where  $f_0$  represents the objective function, i.e., compliance of the structure,  $\mathbf{F}_g$  and  $\mathbf{F}_{\text{ext}}$  are the global force vectors arise due to the self-weight and external loads respectively, and  $SE$  indicates the strain energy.  $\mathbf{K}$  and  $\mathbf{u}$  are the global stiffness matrix and the displacement vector respectively.  $g_1$  and  $g_2$  are constraints.  $V(\mathbf{x})$  and  $V^*$  are the design volume and permitted volume respectively.  $V^* = V_f^* \times \text{Nel}$ , where  $V_f^*$  is the permitted volume fraction.  $\boldsymbol{\lambda}$  (vector),  $\Lambda_1$  (scalar) and  $\Lambda_2$  (scalar) are the Lagrange multipliers corresponding to the state equations,  $g_1$  and  $g_2$  respectively.

Constraint  $g_2$  is formulated using the maximum self-weight determined using the permitted volume,  $F_g^{\max} = gV^*\gamma_s$ , and the intermediate self-weight of the evolving design, wherein  $F_g^e$  indicates self-weight of element  $e$ . This constraint is applied such that a lower bound on the volume fraction can be realized implicitly. Sec. 4.1.1 substantiates the requirement of this constraint for a given volume via numerical examples. The approach retains the constrained nature of the problem. For the finite element analysis, the small elastic deformation is assumed herein.

### 3.2 Sensitivity analysis

A gradient-based optimization technique, the Method of Moving Asymptotes (MMA cf. Svanberg (1987)), is employed to solve the optimization problem mentioned in (14). Thus, derivatives of the objective and constraints with respect to the design variables are required. The derivatives of objective are determined via the adjoint-variable approach. For that, the augmented response  $\mathcal{L}$  is defined using the objective and the state equations as

$$\mathcal{L} = f_0(\mathbf{u}(\bar{\mathbf{x}})) + \boldsymbol{\lambda}^\top (\mathbf{K}(\mathbf{x}) \mathbf{u}(\mathbf{x}) - \mathbf{F}_g(\mathbf{x}) - \kappa \mathbf{F}_{\text{ext}}), \quad (15)$$

where  $\boldsymbol{\lambda}$  is the multiplier vector. We henceforth for brevity omit the arguments from the vector and the matrix quantities. Differentiation of (15) with respect to  $\bar{\mathbf{x}}$  yields

$$\begin{aligned} \frac{\partial \mathcal{L}}{\partial \bar{\mathbf{x}}} &= \frac{\partial f_0}{\partial \bar{\mathbf{x}}} + \frac{\partial f_0}{\partial \mathbf{u}} \frac{\partial \mathbf{u}}{\partial \bar{\mathbf{x}}} + \boldsymbol{\lambda}^\top \left( \frac{\partial \mathbf{K}}{\partial \bar{\mathbf{x}}} \mathbf{u} + \mathbf{K} \frac{\partial \mathbf{u}}{\partial \bar{\mathbf{x}}} - \frac{\partial \mathbf{F}_g}{\partial \bar{\mathbf{x}}} \right) \\ &= \frac{\partial f_0}{\partial \bar{\mathbf{x}}} + \underbrace{\left( \frac{\partial f_0}{\partial \mathbf{u}} + \boldsymbol{\lambda}^\top \mathbf{K} \right)}_{\Theta} \frac{\partial \mathbf{u}}{\partial \bar{\mathbf{x}}} + \boldsymbol{\lambda}^\top \left( \frac{\partial \mathbf{K}}{\partial \bar{\mathbf{x}}} \mathbf{u} - \frac{\partial \mathbf{F}_g}{\partial \bar{\mathbf{x}}} \right). \end{aligned}$$

$\lambda$  is selected such that  $\Theta = 0^3$  that yields,  $\lambda = -2\mathbf{u}$  and thus, with  $f_0 = 2SE$ , one writes

$$\begin{aligned}\frac{\partial \mathcal{L}}{\partial \bar{\mathbf{x}}} &= \frac{\partial f_0}{\partial \bar{\mathbf{x}}} - 2\mathbf{u}^\top \left( \frac{\partial \mathbf{K}}{\partial \bar{\mathbf{x}}} \mathbf{u} - \frac{\partial \mathbf{F}_g}{\partial \bar{\mathbf{x}}} \right) \\ &= -\mathbf{u}^\top \frac{\partial \mathbf{K}}{\partial \bar{\mathbf{x}}} \mathbf{u} + \underbrace{2\mathbf{u}^\top \frac{\partial \mathbf{F}_g}{\partial \bar{\mathbf{x}}}}_{\text{Self-weight sensitivities}}.\end{aligned}\quad (16)$$

In (16), self-weight sensitivities,  $2\mathbf{u}^\top \frac{\partial \mathbf{F}_g}{\partial \bar{\mathbf{x}}}$  appear and they are evaluated using (6). Next, the chain rule (13) is employed to evaluate the objective sensitivities with respect to the design vector, i.e.,  $\frac{\partial f_0}{\partial \bar{\mathbf{x}}}$ . Finding sensitivity of constraint  $g_1$  is straightforward (Sigmund, 2007), whereas that of constraint  $g_2$  can be evaluated using (6). Moreover, it can be noted that compliance objective sensitivities can either be negative or positive (16), i.e., they alter their sign as per the different design variables. This shows the non-monotonous behavior of compliance when self-weight is considered, which is taken care by the MMA optimizer.

## 4 Numerical Examples and Discussions

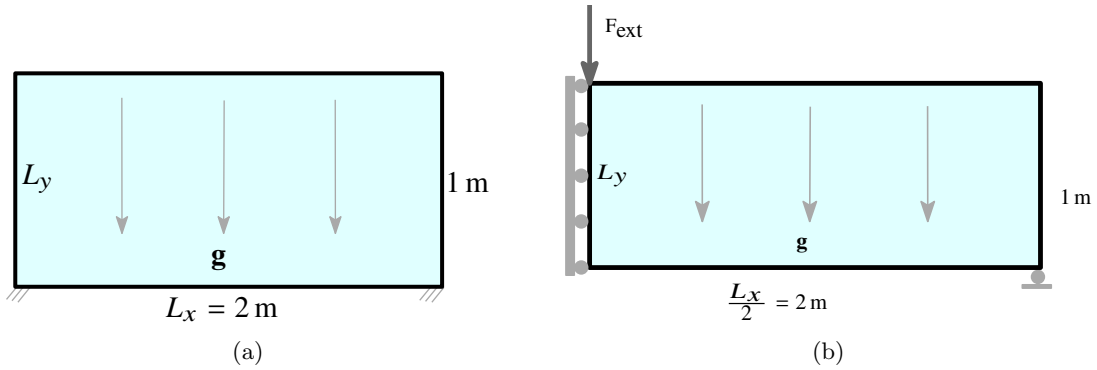


Figure 3: Design domains (a) Example 1: Arch geometry with dimension  $L_x \times L_y = 2 \text{ m} \times 1 \text{ m}$  (b) Example 2: A symmetric MBB beam design with dimension  $\frac{L_x}{2} \times L_y = 2 \text{ m} \times 1 \text{ m}$  is subject to its self-weight and external load  $F_{\text{ext}}$ .  $L_x$  and  $L_y$  indicate the length in  $x$ - and  $y$ -directions respectively. Gravity load  $\mathbf{g}$  is indicated by parallel arrows.  $F_{\text{ext}}$  is an external load.

Herein, the efficacy and robustness of the proposed method is demonstrated by optimizing various structures with self-weight and/or constant external loads. Both, 2D and 3D design settings are considered. The design domains with boundary conditions are displayed in their respective section.  $L_x$ ,  $L_y$  and  $L_z$  are used to indicate length in  $x$ -,  $y$ - and  $z$ -directions respectively. Thickness of the domain is represented by  $t$  which is set to 0.01 m for the presented 2D problems. We use  $N_{\text{ex}} \times N_{\text{ey}}$  bilinear quadrilateral finite elements to describe the 2D design domains, whereas 3D domains are represented via  $N_{\text{ex}} \times N_{\text{ey}} \times N_{\text{ez}}$  hexahedral FEs.  $N_{\text{ex}}$ ,  $N_{\text{ey}}$  and  $N_{\text{ez}}$  denote the total number of FEs employed in  $x$ -,  $y$ - and  $z$ -directions respectively. A density-based TO approach is employed wherein each element is assigned one design variable which is considered constant within the element. TO process is initialized using the given volume fraction. The external move limit of the optimizer is set to 0.1. The Youngs' modulus and mass density of the material are set to 210 GPa and  $7850 \text{ kg m}^{-3}$  respectively (Xu et al., 2013). The total number of the MMA iterations is set to 250 unless otherwise stated. As mentioned earlier,  $\beta$  (11) is doubled after every 25 MMA iterations until it reaches its maximum value 256 and thereafter, it remain so for further iterations.

<sup>3</sup>This is the adjoint equation of the optimization problem (14).



## 4.1 2D design problems

We first present various 2D (benchmark) design-problems experiencing self-weight herein.

### 4.1.1 Example 1: Self-weight loadbearing arch geometry

The design domain for the self-weight loadbearing arch structure is depicted in Fig. 3a. Both ends of the bottom edge are fixed (Fig. 3a), and no external force is applied ( $\kappa = 0$ ).  $L_x = 2$  m and  $L_y = 1$  m are taken. Filter radius is set to  $2.5 \times \max\left(\frac{L_x}{N_{ex}}, \frac{L_y}{N_{ey}}\right)$ . The mass density parameters  $\eta_\gamma = 0.01$  and  $\beta_\gamma = 8$  are used (4). The permitted volume fraction is set to 0.25.

#### Qualifying constraint $g_2$

Problems exclusively with self-weight under a volume constraint lose their constrained nature (Bruyneel and Duysinx, 2005). To prevent this tendency, additional constraint  $g_2$  which implicitly ensures a lower bound on the resource volume in conjunction with the presented mass density interpolation scheme (3) and employed three-field density representation technique is considered. The constraint is qualified and substantiated its importance by optimizing the arch design (Fig. 3a) with self-weight (14) using different cases.

To parameterize the design domain, (i)  $N_{ex} \times N_{ey} = 100 \times 50$  FEs and (ii)  $N_{ex} \times N_{ey} = 200 \times 100$  FEs are used. This is done to record the behavior of the approach with respect to different mesh sizes. In addition, though the problem is symmetric, the full model is considered to note any tendency to lose the symmetry in the optimized design. Four cases namely, (i) CASE I:  $100 \times 50$  FEs without constraint  $g_2$ , (ii) CASE II:  $100 \times 50$  FEs with constraint  $g_2$ , (iii) CASE III:  $200 \times 100$  FEs without constraint  $g_2$ , and (iv) CASE IV:  $200 \times 100$  FEs with constraint  $g_2$  are considered.

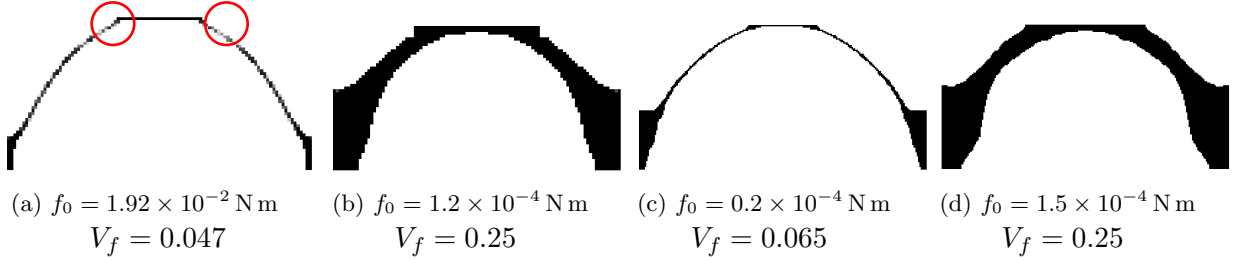


Figure 4: The optimized results to Example 1 with various cases. (a) CASE I:  $100 \times 50$  FEs without constraint  $g_2$  (b) CASE II:  $100 \times 50$  FEs with constraint  $g_2$ , (c) CASE III:  $200 \times 100$  FEs without constraint  $g_2$ , (d) CASE IV:  $200 \times 100$  FEs with constraint  $g_2$ . The optimized solution displayed in (a) is disconnected as encircled in red.  $V_f$  indicates the obtained volume fraction at the end of optimization.

The optimized results for all the cases are displayed after 250 MMA iterations in Fig. 4. When constraint  $g_2$  is not taken into account, for example in CASE I and CASE III, the optimization problem becomes unconstrained as evident from their volume constraint convergence plots (see Fig. 5a and Fig. 5b). The optimized design of CASE I contains gray elements (marked in red circles in Fig. 4a). On the other hand, with constraint  $g_2$  (CASE II and CASE IV) the optimization problem retains its constrained nature and at the end of TO, volume constraint  $g_1$  stays active (Fig. 5a and Fig. 5b). Steps in volume fraction convergence curves are due to  $\beta$  updation scheme (11) which is performed to achieve 0-1 optimized solutions (Wang et al., 2011). Constraints convergence plots for CASE II and CASE IV are displayed in Fig. 6a

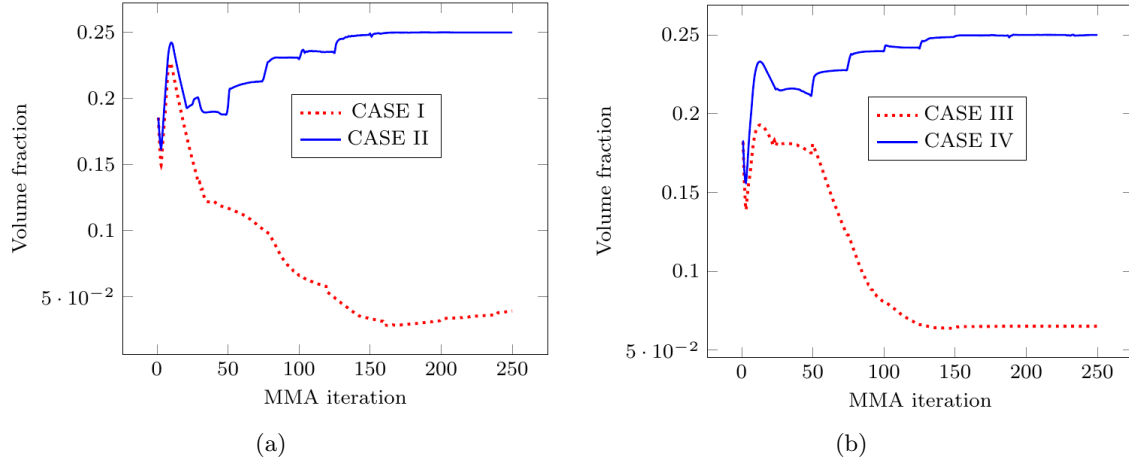


Figure 5: Volume fraction convergence plots for CASE I, CASE II, CASE III, CASE IV.

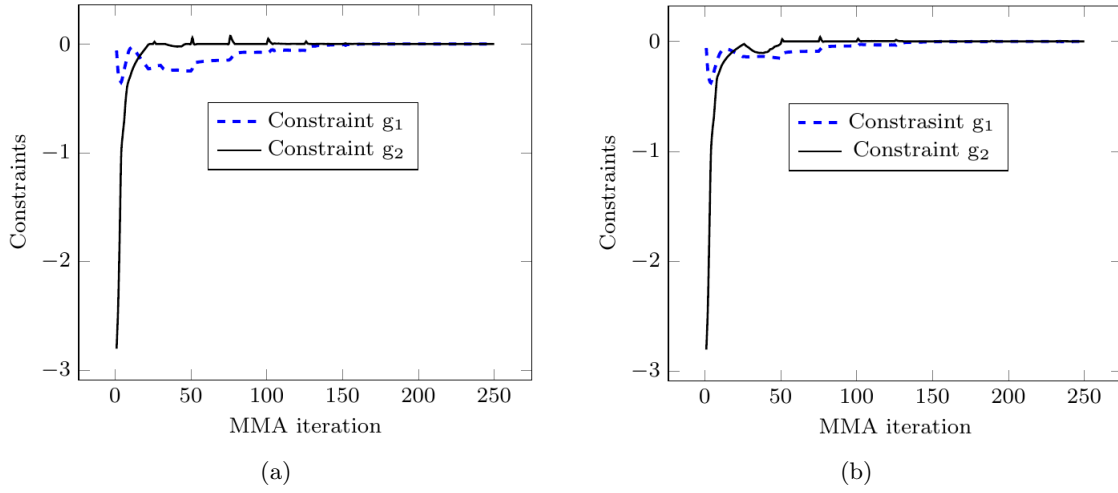


Figure 6: Constraints convergence plots. (a) CASE II and (b) CASE IV.

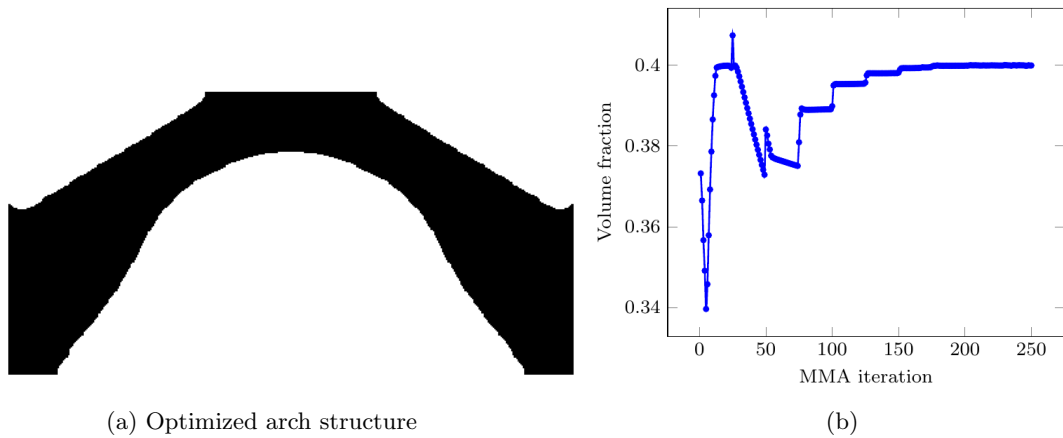


Figure 7: (a) Optimized arch design,  $V_f = 0.40$ ,  $f_0 = 4.7 \times 10^{-4}$  N m, (b) Volume fraction convergence curve

and Fig. 6b respectively. Constraints are active at the end of optimization. The optimized designs of CASE II (Fig. 4b) and CASE IV (Fig. 4d) are close to 0-1 solutions. Topologies of these solutions resemble those reported in (Bruyneel and Duysinx, 2005; Huang and Xie,

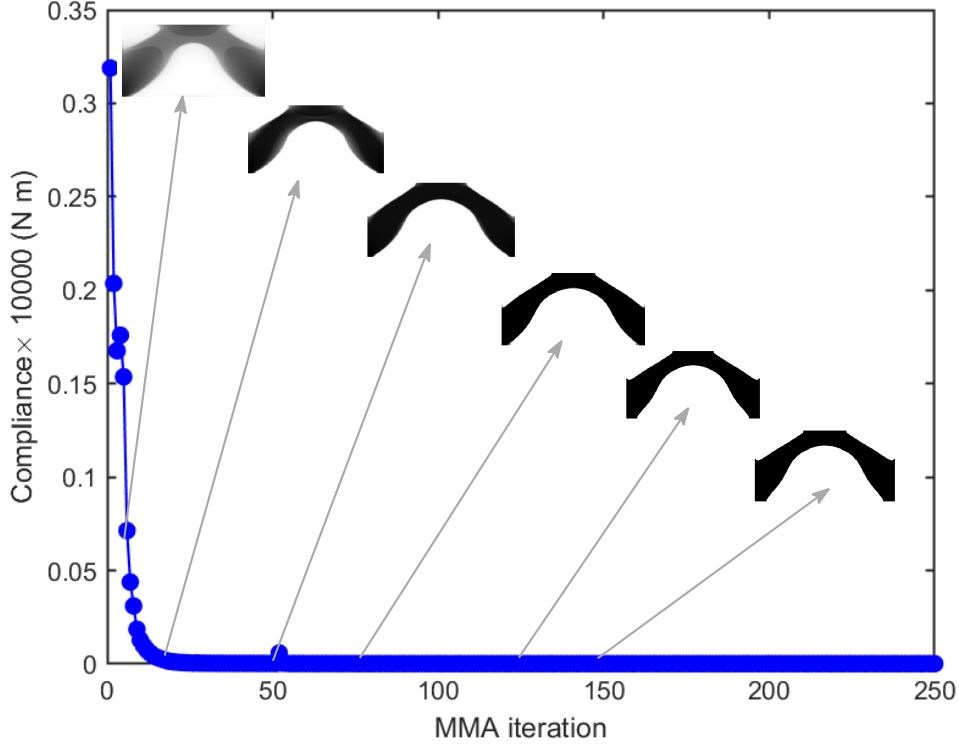


Figure 8: Objective convergence history of the arch structure with intermediate results.

2011; Novotny et al., 2021). Furthermore, these solutions (Fig. 4b and Fig. 4d) are symmetric with respect to the central  $y$ -axis of the domain and thus, symmetry nature of the problem is retained. We henceforth solve all problems with constraint  $g_2$  and report convergence history for constraint  $g_1$  only in view of Fig. 6.

#### 4.1.2 Arch structure

The design domain (Fig. 3a) is described using  $N_{ex} \times N_{ey} = 400 \times 200$  FEs. The volume fraction is set to 0.40.  $\eta_\gamma = 0.1$  and  $\beta_\gamma = 8$  are considered. Filter radius is set to  $3.5 \max\left(\frac{L_x}{N_{ex}}, \frac{L_y}{N_{ey}}\right)$ . Other design parameters are same as those employed in Sec. 4.1.1.

The optimized result is depicted in Fig. 7a, and the corresponding convergence curves for the volume fraction the objective are displayed in Fig. 7b and Fig. 8 respectively. The design evolution at different intermediate stages are also shown (Fig. 8). The objective convergence is smooth and relatively rapid. As  $\beta$  increases, the boundaries of the solution become crisp, and the optimized solution moves towards 0-1 design (Fig. 8). The volume constraint is active and satisfied at the end of optimization and thus, constrained nature of the problem is maintained. As  $\beta$  (11) is updated at every 25 MMA iterations, corresponding steps in volume fraction can be noted (Fig. 7b).

#### 4.1.3 Example 2

A Messerschmitt-Blkow-Blohm (MBB) beam design subject to self-weight as well as an external load is studied in this example.

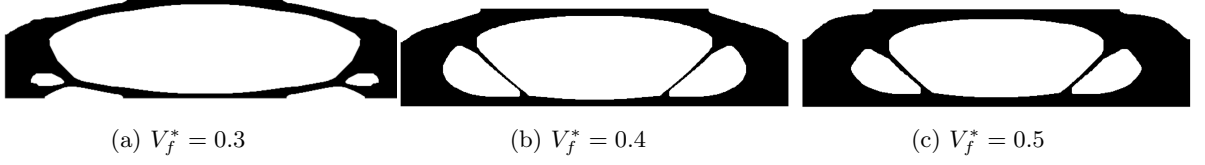


Figure 9: Optimized designs for the MBB beam design

In view of symmetric nature of the problem, the right symmetric part (Fig. 3b) with dimension  $\frac{L_x}{2} = 2$  m and  $L_y = 1$  m is considered. Magnitudes of the external load, applied as shown in Fig. 3b in the negative  $y$ -direction, are set to  $\kappa F_g^{\max}$  with  $\kappa = [0, 1]$ . The boundary conditions of the problem are as depicted in Fig. 3b. The domain is parameterized using  $N_{\text{ex}} \times N_{\text{ey}} = 320 \times 160$  FEs. The filter radius is set to  $3 \times \max\left(\frac{L_x}{N_{\text{ex}}}, \frac{L_y}{N_{\text{ey}}}\right)$ . Other parameters are same as used in Sec. 4.1.1. In this study, two main cases are considered.

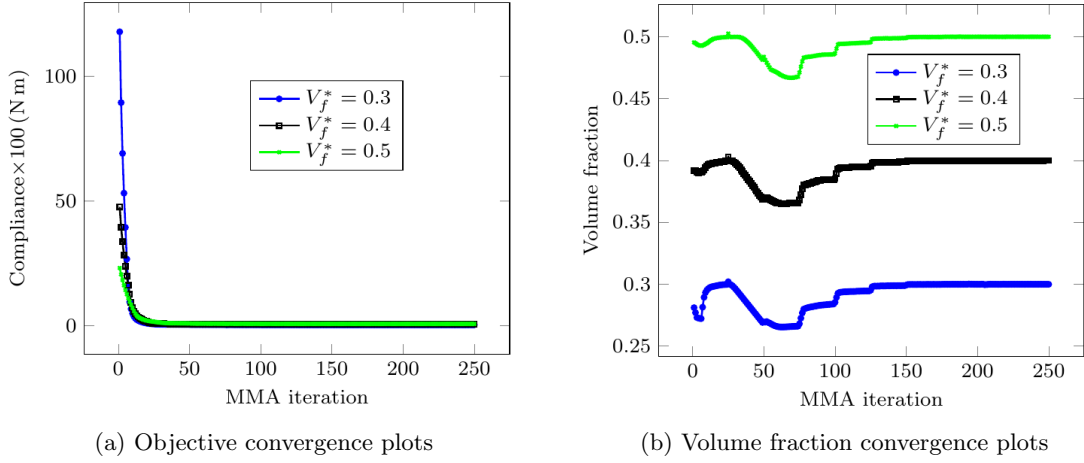


Figure 10: Converge plots for the compliance and different volume fractions.

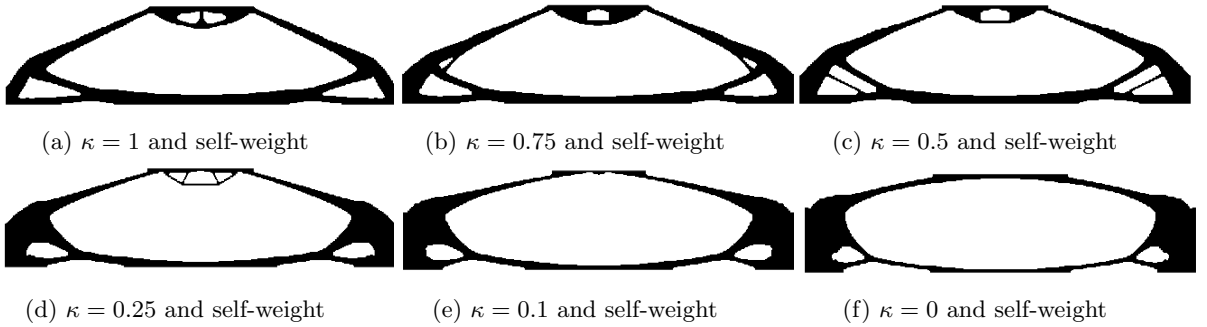


Figure 11: Optimized results to the MBB beam with different  $\kappa$ . (a)  $f_0 = 3.83 \times 10^{-2}$  N m, (b)  $f_0 = 2.64 \times 10^{-2}$  N m, (c)  $f_0 = 1.73 \times 10^{-2}$  N m, (d)  $f_0 = 0.83 \times 10^{-2}$  N m, (e)  $f_0 = 0.45 \times 10^{-2}$  N m, (f)  $f_0 = 0.24 \times 10^{-2}$  N m

First, the beam is optimized with  $\kappa = 0$ , i.e., only self-weight and different volume fractions e.g.  $V_f^* = 0.3, 0.4, 0.5$ . The optimized results are displayed in Figs. 9a-9c, which are very close to 0-1 with similar topologies. Each optimized design has a horizontal bar-typed slender member which is expected with such boundary conditions. As volume fraction increases more material get accumulated near the support in the optimized structures (Figs. 9a-9c). This occurs to reduce the bending moment of self-weight of the material placed by the optimizer. Convergence curves of the objectives and the volume fractions are depicted in Fig. 10a and

Fig. 10b respectively. The objective convergence is smooth and rapid (Fig. 10a) that is also noted previously. Constrained nature of the problem is preserved as the volume constraint is active at the end of optimization (Fig. 10b). Moreover, the trends of volume fraction convergence plots are similar as the employed  $\beta$  continuation is same of them. The steps in volume convergence curves (Fig. 10b) are associated with  $\beta$  updation.

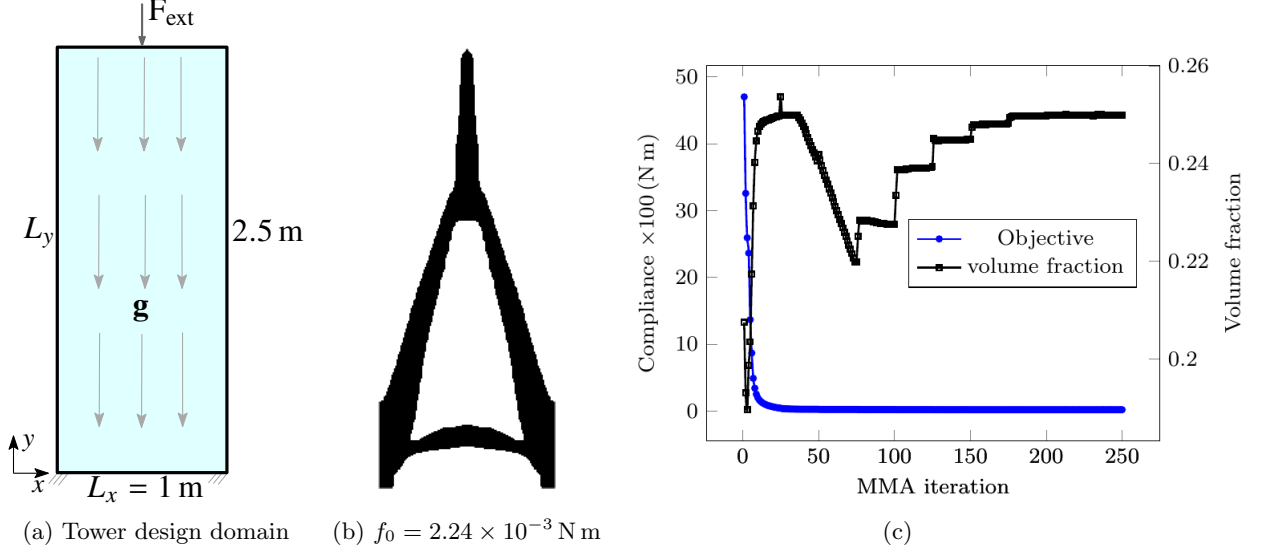


Figure 12: (a) Design domain of dimension  $L_x \times L_y = 1 \text{ m} \times 2.5 \text{ m}$  is under its self-weight and external load  $F_{ext}$ , (b) Optimized design for  $V_f = 0.25$ , (c) Convergence curves for the objective and volume fraction.

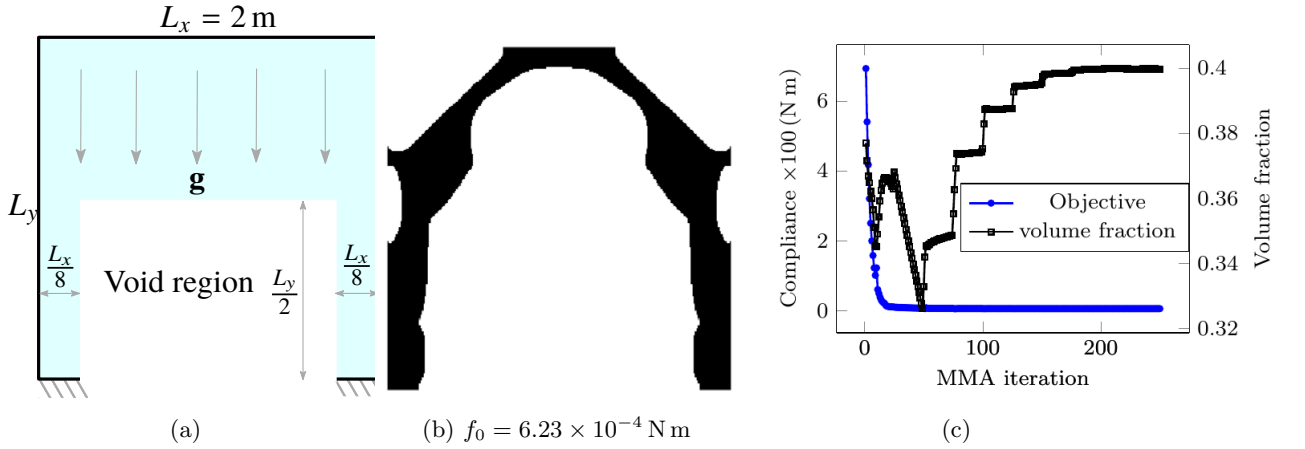


Figure 13: (a) Design domain of dimension  $L_x \times L_y = 2 \text{ m} \times 2 \text{ m}$  is subject to its self-weight. A non-design void region of dimension  $\frac{7L_x}{4} \times \frac{L_y}{2}$  is present (b) Optimized design, (c) Convergence curves for the objective and volume fraction.

Next, we solve the MBB beam design with different magnitudes of  $F_{ext}$ , i.e., with different  $\kappa$ . The desired resource volume is set to 25%. Other parameters are same as above. The optimized results are shown in Fig. 11. One can note that as  $\kappa$  decreases, the material gets transferred from the center region to the lateral sides of the domain so that the optimized designs experience less bending moment due to self-weight. The central structures which support the external load disappear eventually as magnitude of  $F_{ext}$  is decreased. The geometry of the optimized layout gradually changes to two connected arch structures facing towards each other. The final compliance decreases as  $\kappa$  decreases that is as expected. The convergence of objective is found to be smooth and rapid. The volume fractions are satisfied and remain active for all  $\kappa$ .

#### 4.1.4 Example 3

For this example, a design domain for tower structure is consider with self-weight and an external load.

The design domain is displayed in Fig. 12a. Both ends of the bottom edge are fixed.  $L_x \times L_y = 1 \text{ m} \times 2.5 \text{ m}$  is taken. Filter radius is equal to  $5.6 \times \max\left(\frac{L_x}{N_{ex}}, \frac{L_y}{N_{ey}}\right)$ . In light of the vertical symmetry, only a symmetric half design domain is consider for simulation and optimization.  $110 \times 550$  FEs are employed to parameterize the symmetric half domain. Volume fraction is set to 0.25. Magnitude of the external load is taken equal to the self-weight. The load is applied at the center of the top edge of domain in the negative  $y$ -direction. Other design parameters are same as above.

The optimized tower structure is shown in Fig. 12b. The objective and the volume fraction convergence plots are displayed in Fig. 12c. A rapid and smooth convergence in the objective can be noted. The volume fraction is satisfied and remains active at the end of optimization. The optimized structure is close to 0-1. A vertical slender structure appears in the optimized design (Fig. 12b) to contain the applied external load. By and large, the optimized design resemble a typical tower design.

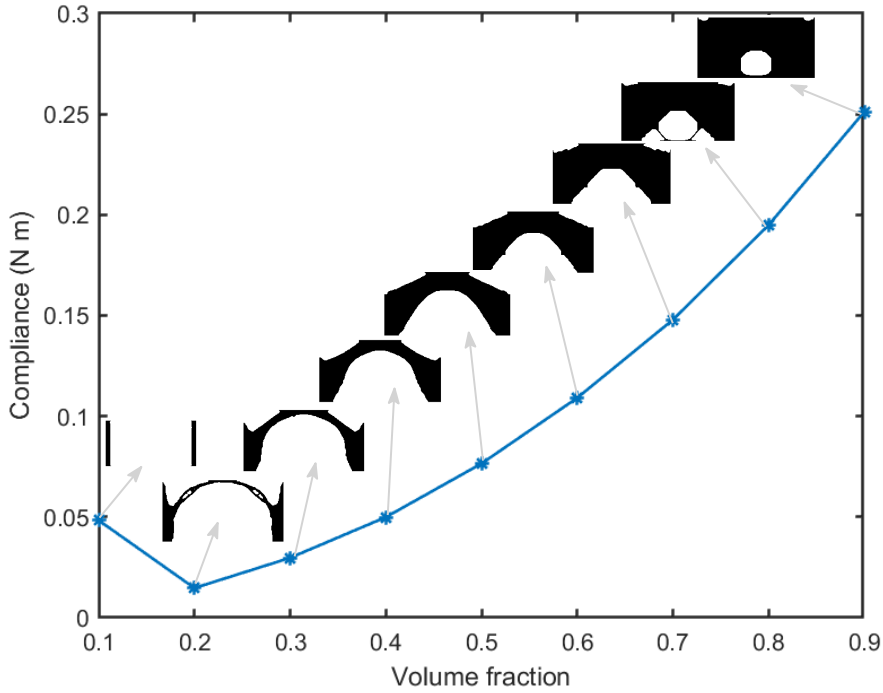


Figure 14: A Pareto curve and optimized arch designs for different volume fraction

#### 4.1.5 Example 4

In this example, the method is demonstrated by designing a structure resembling a typical house arch structure.

The design domain and boundary conditions are shown in Fig. 13a wherein  $L_x \times L_y = 2 \text{ m} \times 2 \text{ m}$ . A non-design void region of size  $\frac{7L_x}{4} \times \frac{L_y}{2}$  (Fig. 13a) is present in the design domain to facilitate entry and exit. The structure is considered under self-weight only, i.e.,  $\kappa = 0$ . Though a

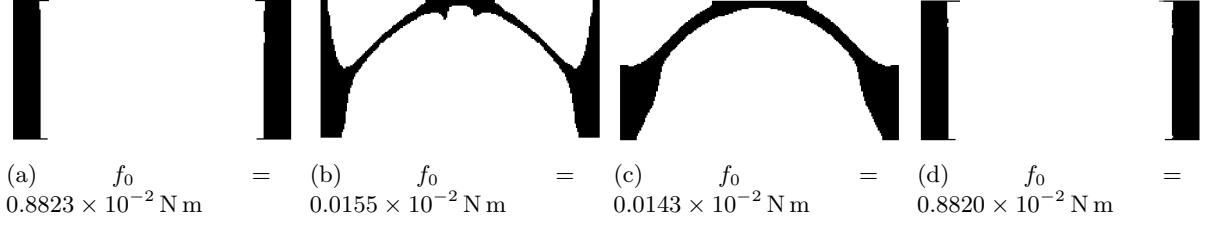


Figure 15: Optimized results. (a)  $\eta_\gamma = 0.1$ ,  $\beta_\gamma = 10$ , (b)  $\eta_\gamma = 0.05$ ,  $\beta_\gamma = 10$ , (c)  $\eta_\gamma = 0.01$ ,  $\beta_\gamma = 10$ , and (d)  $\eta_\gamma = 0.1$ ,  $\beta_\gamma = 20$

vertical symmetry exists, we take full domain to analyze and optimize so that any deviation from symmetry can be noted in presence of a non-design domain. The domain is parameterized by  $N_{\text{ex}} \times N_{\text{ey}} = 240 \times 240$  FEs. The permitted volume fraction is 0.40. Filter radius is set to  $3.6 \times \max\left(\frac{L_x}{N_{\text{ex}}}, \frac{L_y}{N_{\text{ey}}}\right)$ . Other parameters are same as those used above.

The optimized result is displayed in Fig. 13b. The optimized design is constituted via two pillars and an arch structure on the top. The corresponding convergence plots are depicted in Fig. 13c. As noted earlier here too the objective convergence is rapid and smooth. One can note that the volume constraint is active at the end of optimization. This indicates that method works well when non-design domains are present.

## 4.2 Parameter study

In this section, we present the effect of different parameters on the optimized designs with self-weight.

### 4.2.1 Volume fraction

Herein, different volume fractions ranging from 0.1 to 0.9 are used to solve the arch structure (Fig. 3a).  $N_{\text{ex}} \times N_{\text{ey}} = 200 \times 100$  FEs is used to represent the design domain.  $\beta_\gamma = 6$  and  $\eta_\gamma = 0.01$  are considered. Filter radius is set to  $2.5 \times \max\left(\frac{L_x}{N_{\text{ex}}}, \frac{L_y}{N_{\text{ey}}}\right)$ . Other design parameters are same as those used in Sec. 4.1.1.

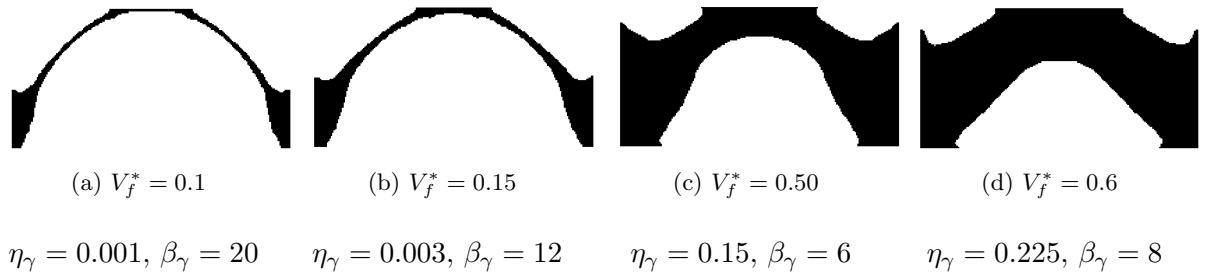


Figure 16: Optimized results. (a)  $f_0 = 4.6 \times 10^{-5}$  N m, (b)  $f_0 = 8.7 \times 10^{-5}$  N m, (c)  $f_0 = 7.69 \times 10^{-4}$  N m, and (d)  $f_0 = 1.1 \times 10^{-3}$  N m

Fig. 14 displays a Pareto curve between compliance and volume fractions. As volume fraction increases, self-weight of the optimized design increases and thus, corresponding compliance increases. The optimized results are shown in Fig. 14 for every volume fraction. It is noted that the volume constraint for each case remains active at the end of optimization, and the corresponding objective convergence is rapid and smooth. The optimized design with volume

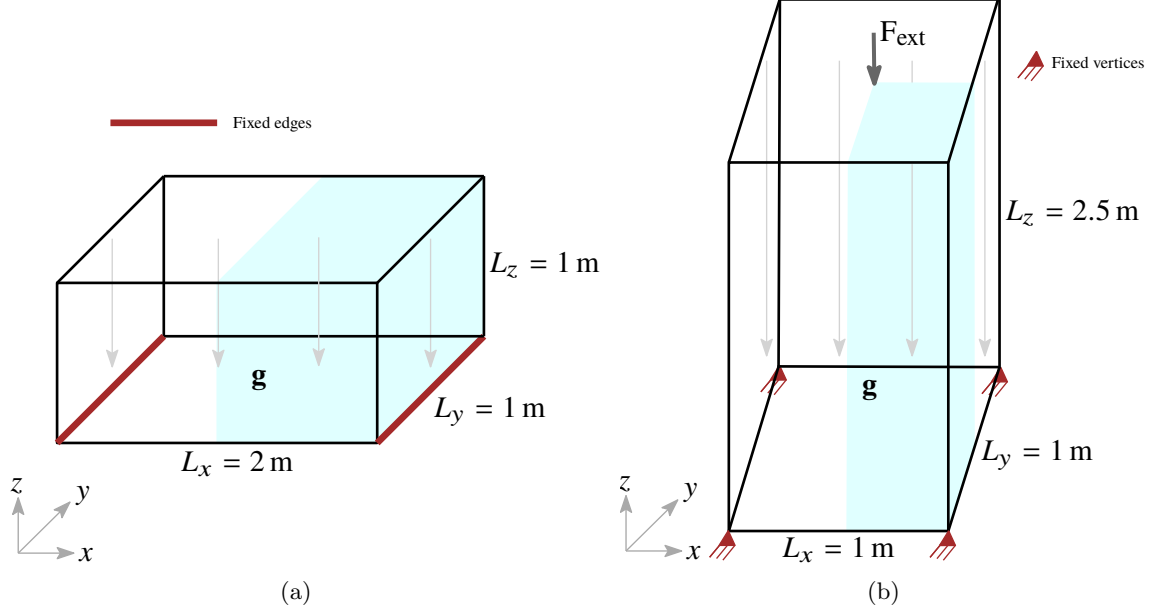


Figure 17: 3D design domains. (a) Arch structure domain and (b) Tower design domain. Gravity is indicated via gray parallel arrows pointing in the negative  $z$ -direction.

fraction 0.1 is disconnected, which is constituted via two pillars (see Sec. 4.2.2). Compliance with  $V_f^* = 0.1$  is obtained higher than that with  $V_f^* = 0.2$ .

#### 4.2.2 Mass density parameters

This study demonstrates the effect of different mass density parameters  $\{\eta_\gamma, \beta_\gamma\}$  on the optimized designs with self-weight.

The design domain for this study is shown in Fig. 3a. Volume fraction  $V_f^* = 0.20$  is set, and filter radius is taken equal to  $2.5 \times \max\left(\frac{L_x}{N_{\text{ex}}}, \frac{L_y}{N_{\text{ey}}}\right)$ .  $N_{\text{ex}} \times N_{\text{ey}} = 200 \times 100$  FEs is employed to describe the design domain. Note that,  $\beta_\gamma$  controls the slope of material density interpolation (Fig. 2). For higher  $\beta_\gamma$ , elements with  $\bar{x} \geq \eta_\gamma$  act as solid FEs.

The optimized designs with various  $\{\eta_\gamma, \beta_\gamma\}$  are depicted in Fig. 15. Topologies of the optimized designs are similar in Fig. 15b and Fig. 15c but having different final objective values. The obtained final objective value with  $\{\eta_\gamma, \beta_\gamma\} = \{0.01, 20\}$  is lower than all other cases considered, which suggests that indeed an arch-shaped structure is the actual optimized design for the problem shown in Fig. 3a. Optimized designs shown in Fig. 15a, Fig. 15d are disconnected, and their final compliance are higher than the other two in Fig. 15. When decreasing  $\eta_\gamma$  and increasing  $\beta_\gamma$ , the region of transitions from void to solid reduces (Fig. 2) and in those cases, the optimized designs are found to be connected and sensible. Relatively moderate  $\beta_\gamma$  and  $\eta_\gamma$  offers smoother optimization problem, however the final obtained designs may be disconnected. Thus, in general,  $\beta_\gamma$  and  $\eta_\gamma$  can be chosen such that a suitable trade-off between the differentiability and transition can be obtained. By and large, based on our experience,  $\eta_\gamma$  close to  $(V_f^*)^p$  and  $\beta_\gamma$  between 5 – 20 ensure the desired trade-off. To demonstrate that indeed the recommended values work, we solve the problem for permitted volume fractions 0.1, 0.15, 0.5 and 0.6 with  $\{0.001, 20\}$ ,  $\{0.003, 12\}$ ,  $\{0.15, 6\}$ ,  $\{0.225, 8\}$  as their  $\{\eta_\gamma, \beta_\gamma\}$ . Fig. 16 shows the optimized design. These designs are connected and sensible. In addition, the volume constraints for all cases are found to be satisfied and active at the end of optimization.



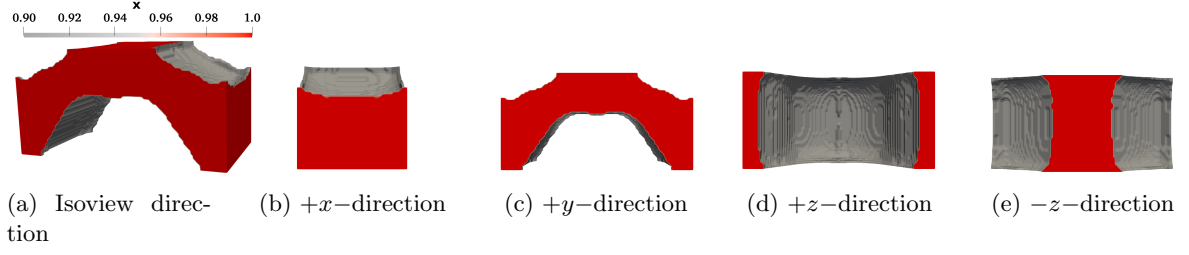


Figure 18: 3D Optimized results for the arch geometry are shown in different view directions.

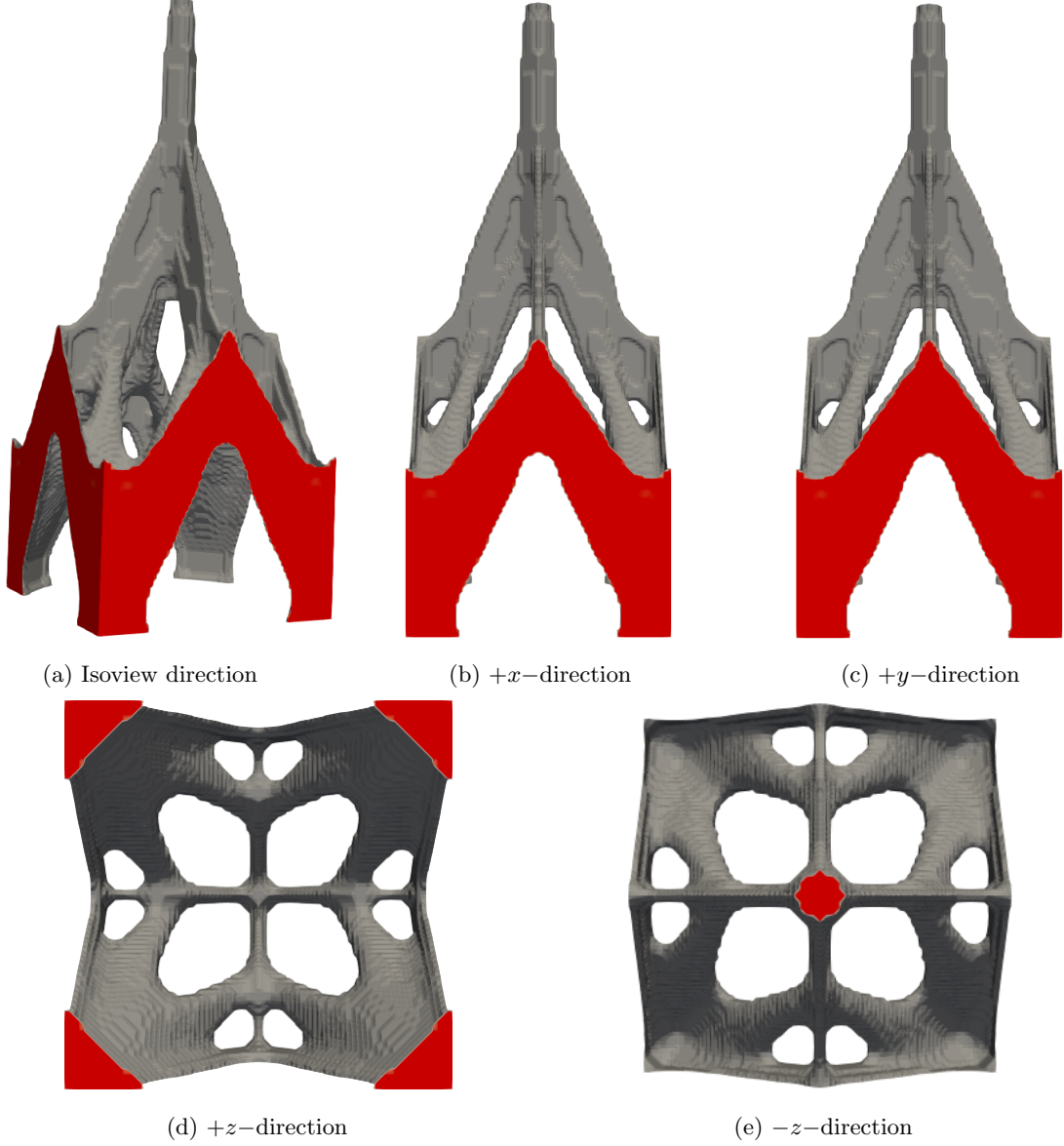


Figure 19: 3D Optimized results for a tower structure are displayed in different view directions.

### 4.3 Three-dimensional examples

This section demonstrates that the proposed approach can without much difficulty be extended for 3D problems including self-weight. TO is performed using an in-house MATLAB code wherein the conjugate gradient method in association with incomplete Cholesky preconditioning

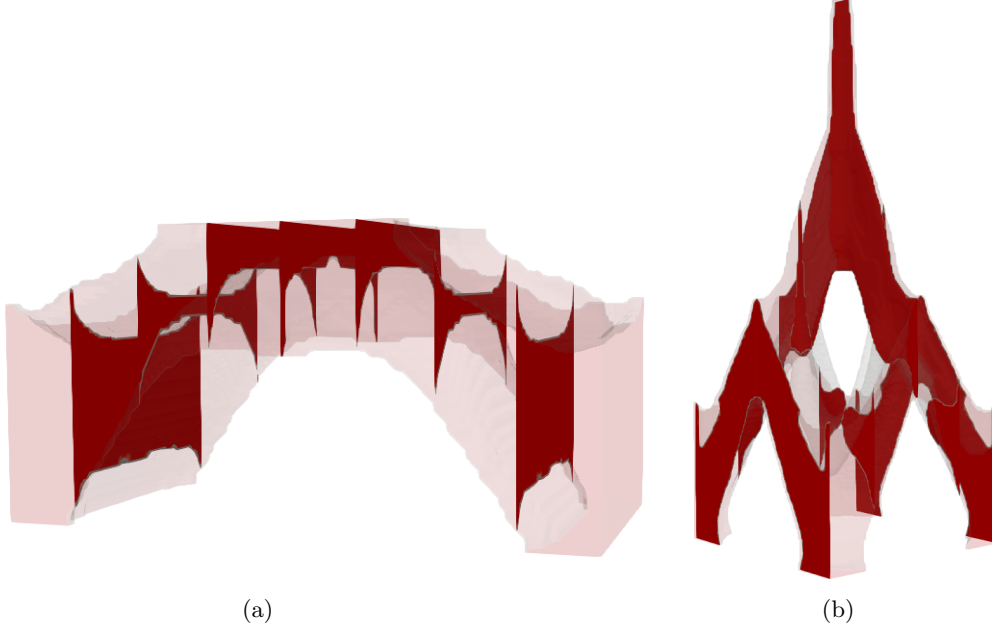


Figure 20: Material distributions for different cross-sections in arbitrary directions (a) Arch structure (b) Tower structure.

is employed to solve the linear system from the equilibrium and adjoint equation.

Two 3D problems are solved: (i) an arch structure problem with only self-weight and (ii) a tower structure with self-weight and a central constant load. Their design domains are displayed in Fig. 17. For the arch structure, we exploit one symmetry axis for the analysis and optimization (Fig. 17a), whereas for the tower problem both symmetry axes are exploited (Fig. 17b). The symmetric parts used for optimization are shadowed using lightcyan color (Fig. 17).

$L_x \times L_y \times L_z = 2\text{ m} \times 1\text{ m} \times 1\text{ m}$  and  $L_x \times L_y \times L_z = 1\text{ m} \times 1\text{ m} \times 2.5\text{ m}$  are considered for the arch design (Fig. 17a) and the tower design (Fig. 17b) respectively. The half symmetric part of arch domain (colored shape in Fig. 17a) is parameterized via  $N_{\text{ex}} \times N_{\text{ey}} \times N_{\text{ez}} = 50 \times 50 \times 50$  hexahedral FEs, whereas the quarter part of the tower domain (colored shape in Fig. 17b) is described via  $N_{\text{ex}} \times N_{\text{ey}} \times N_{\text{ez}} = 40 \times 40 \times 200$  FEs. The permitted volume fractions, filter radii and material density parameters  $\{\eta_\gamma, \beta_\gamma\}$  for arch and tower design problems are set to 0.35% and 0.1%,  $4.8 \times \max\left(\frac{L_x}{N_{\text{ex}}}, \frac{L_y}{N_{\text{ey}}}, \frac{L_z}{N_{\text{ez}}}\right)$  and  $2\sqrt{3} \times \max\left(\frac{L_x}{N_{\text{ex}}}, \frac{L_y}{N_{\text{ey}}}, \frac{L_z}{N_{\text{ez}}}\right)$ , and  $\{0.01, 8\}$  and  $\{0.001, 8\}$  respectively. Other design parameters are same as those used above.

Figure 18 and Fig. 19 show the optimized arch and tower designs in different view directions respectively. An isosurface with the physical density value at 0.90 is taken to plot the optimized results. The results in an isoview direction are displayed in Fig. 18a and Fig. 19a respectively. It can be noted that  $+y$ -direction view of the optimized 3D arch result (Fig. 18c) resembles that obtained for 2D arch structure (Fig. 7a). For both designs, the optimizer has succeeded in providing the optimized shape which can be more advantageous for the compliance objective. The material distribution pertaining to different cross-sections for the arch and tower structures are shown in Fig. 20a and Fig. 20b respectively. It can be noticed that the material distributions at the cross-sectional areas are close to 1.0 indicating that the optimized results are closed to binary. In addition, the results render clear design interpretation. We can expect relatively more detailed features in the optimized tower design with much finer mesh which can be efficiently obtained using fully parallelized framework, which forms one of the future works.

## 5 Closure

This paper presents a novel density-based topology optimization approach to optimize continua subject to self-weight. The robustness and versatility of the approach is demonstrated by optimizing various structures pertaining to 2D and 3D dimensions. The compliance of the structure is minimized with a given volume constraint and a conceptualized constraint.

One of the challenges for the design problems involving self-weight is the tendency to lose their constrained nature. In the presented method, the mass density of each element is interpolated using a smooth Heaviside projection function. This facilitates a smooth representation of the self-weight and thus, corresponding load sensitivities are evaluated readily using the adjoint-variable method. In addition, this helps formulate an additional constraint for implicitly imposing a lower bound on the permitted resource volume of the domain. The given volume fraction for the problem gets satisfied and remains active at the end of the optimization, i.e., constrained behavior of the problem is retained. The mass density parameters are selected *a priori* to the optimization that affect the optimized topologies. The recommended values are provided based on the numerical examples solved.

The modified SIMP material interpolation method is employed in conjunction with a three-field density representation technique. Parameter  $\beta$  is increased using a continuation scheme such that the optimized designs steer toward close to 0-1 solutions. Consequently, the parasitic effects which arise typically due to low-stiffness elements is circumvented. The presented approach works well with designs containing non-design domains as it is shown via a house arch design containing a non-design void region and maintains symmetric nature of problem in the optimized structures. The approach is easily extended to 3D problem settings that is demonstrated via two three-dimensional problems. A 3D arch structure experiencing only self-weight and a 3D tower structure experiencing both self-weight and external load are optimized and presented. It is noted that convergence of the objective is smooth and rapid for all the problems and the corresponding volume constraints remain active at the end of optimization. The optimized results provide clear design interpretation.

## Acknowledgment

The author would like to thank Professor G. K. Ananthasuresh for fruitful discussions, Professor Krister Svanberg for providing MATLAB codes of the MMA optimizer and acknowledge financial support from the Science & Engineering research board, Department of Science and Technology, Government of India under the project file number R/JF/2020/000023.

## References

- Bruns TE, Tortorelli DA (2001) Topology optimization of non-linear elastic structures and compliant mechanisms. *Computer methods in applied mechanics and engineering* 190(26-27):3443–3459
- Bruyneel M, Duysinx P (2005) Note on topology optimization of continuum structures including self-weight. *Structural and Multidisciplinary Optimization* 29(4):245–256
- Chang C, Chen A (2014) The gradient projection method for structural topology optimization including density-dependent force. *Structural and Multidisciplinary Optimization* 50(4):645–657

- Cook RD, Malkus DS, Plesha ME, Witt RJ (2007) Concepts and applications of finite element analysis. John Wiley & sons
- Félix L, Gomes AA, Suleman A (2020) Topology optimization of the internal structure of an aircraft wing subjected to self-weight load. *Engineering Optimization* 52(7):1119–1135
- Guest JK, Prévost JH, Belytschko T (2004) Achieving minimum length scale in topology optimization using nodal design variables and projection functions. *International journal for numerical methods in engineering* 61(2):238–254
- Holmberg E, Thore CJ, Klarbring A (2015) Worst-case topology optimization of self-weight loaded structures using semi-definite programming. *Structural and Multidisciplinary Optimization* 52(5):915–928
- Huang X, Xie Y (2011) Evolutionary topology optimization of continuum structures including design-dependent self-weight loads. *Finite Elements in Analysis and Design* 47(8):942–948
- Kumar P, Langelaar M (2021) On topology optimization of design-dependent pressure-loaded three-dimensional structures and compliant mechanisms. *International Journal for Numerical Methods in Engineering* 122(9):2205–2220
- Kumar P, Frouws J, Langelaar M (2020) Topology optimization of fluidic pressure-loaded structures and compliant mechanisms using the darcy method. *Structural and Multidisciplinary Optimization* 61(4)
- Lazarov BS, Wang F, Sigmund O (2016) Length scale and manufacturability in density-based topology optimization. *Archive of Applied Mechanics* 86(1-2):189–218
- Lee E, James KA, Martins JR (2012) Stress-constrained topology optimization with design-dependent loading. *Structural and Multidisciplinary Optimization* 46(5):647–661
- Novotny A, Lopes C, Santos R (2021) Topological derivative-based topology optimization of structures subject to self-weight loading. *Structural and Multidisciplinary Optimization* 63(4):1853–1861
- Pedersen NL (2000) Maximization of eigenvalues using topology optimization. *Structural and multidisciplinary optimization* 20(1):2–11
- Rozvany GI (1977) Optimal plastic design: allowance for self-weight. *Journal of the Engineering Mechanics Division* 103(6):1165–1170
- Sigmund O (2007) Morphology-based black and white filters for topology optimization. *Structural and Multidisciplinary Optimization* 33(4-5):401–424
- Sigmund O, Maute K (2013) Topology optimization approaches. *Structural and Multidisciplinary Optimization* 48(6):1031–1055
- Stolpe M, Svanberg K (2001) An alternative interpolation scheme for minimum compliance topology optimization. *Structural and Multidisciplinary Optimization* 22(2):116–124
- Svanberg K (1987) The method of moving asymptotes—a new method for structural optimization. *International journal for numerical methods in engineering* 24(2):359–373
- Trillet D, Duysinx P, Fernandez Sanchez EF (2021) Analytical relationships for imposing minimum length scale in the robust topology optimization formulation. *Structural and Multidisciplinary Optimization*

- Wang F, Lazarov BS, Sigmund O (2011) On projection methods, convergence and robust formulations in topology optimization. *Structural and Multidisciplinary Optimization* 43(6):767–784
- Xu H, Guan L, Chen X, Wang L (2013) Guide-weight method for topology optimization of continuum structures including body forces. *Finite Elements in Analysis and Design* 75:38–49
- Zhang S, Li H, Huang Y (2021) An improved multi-objective topology optimization model based on simp method for continuum structures including self-weight. *Structural and Multidisciplinary Optimization* 63(1):211–230
- Zhang W, Zhao L, Gao T (2017) Cbs-based topology optimization including design-dependent body loads. *Computer Methods in Applied Mechanics and Engineering* 322:1–22